The Astrophysical Journal Supplement Series, 246:29 (12pp), 2020 February https://doi.org/10.3847/1538-4365/ab5221

Solar Energetic Particles Produced by a Slow Coronal Mass Ejection at ∼0.25 au

J. Giacalone[1], D. G. Mitchell[2], R. C. Allen[2], M. E. Hill[2], R. L. McNutt, Jr.[2], J. R. Szalay[3], M. I. Desai[4], A. P. Rouillard[5], A. Kouloumvakos[5], D. J. McComas[3], E. R. Christian[6], N. A. Schwadron[3,7], M. E. Wiedenbeck[8], S. Bale[9,10,11,12], L. E. Brown[2], A. Case[13], X. Chen[1], C. M. S. Cohen[14], C. Joyce[3], J. C. Kasper[15], K. G. Klein[1], K. Korreck[13], D. E. Larson[10], R. Livi[10], R. A. Leske[14], R. J. MacDowall[16], W. H. Matthaeus[17], R. A. Mewaldt[14], T. Nieves-Chinchilla[6], M. Pulupa[10], E. C. Roelof[2], M. L. Stevens[13], A. Szabo[6], and P. L. Whittlesey[10]
[1] Lunar & Planetary Laboratory, University of Arizona, Tucson, AZ 85721, USA
[2] Applied Physics Laboratory, Laurel, MD 20723, USA
[3] Department of Astrophysical Sciences, Princeton University, Princeton, NJ 08544, USA
[4] University of Texas at San Antonio, San Antonio, TX 78249, USA
[5] IRAP/CRNS, Toulouse, France
[6] Heliophysics Science Division, NASA/Goddard Space Flight Center, Greenbelt, MD 20771, USA
[7] University of New Hampshire, Durham, NH 03824, USA
[8] Jet Propulsion Laboratory, California Institute of Technology, Pasadena, CA 91109, USA
[9] Physics Department, University of California at Berkeley, Berkeley, CA 94720-7300, USA
[10] Space Sciences Laboratory, University of California, Berkeley, CA 94720-7450, USA
[11] The Blackett Laboratory, Imperial College London, London, SW7 2AZ, UK
[12] School of Physics and Astronomy, Queen Mary University of London, London E1 4NS, UK
[13] Harvard-Smithsonian Center for Astrophsyics, Cambridge, MA 02138, USA
[14] California Institute of Technology, Pasadena, CA 91125, USA
[15] University of Michigan, Ann Arbor, MI 48109, USA
[16] Solar System Exploration Division, NASA/Goddard Space Flight Center, Greenbelt, MD 20771, USA
[17] University of Delaware, Newark, DE 19716, USA
Received 2019 September 12; revised 2019 October 24; accepted 2019 October 27; published 2020 February 3

Abstract

We present an analysis of *Parker Solar Probe* (*PSP*) IS⊙IS observations of ∼30–300 keV n^{-1} ions on 2018 November 11 when *PSP* was about 0.25 au from the Sun. Five hours before the onset of a solar energetic particle (SEP) event, a coronal mass ejection (CME) was observed by *STEREO-A*/COR2, which crossed *PSP* about a day later. No shock was observed locally at *PSP*, but the CME may have driven a weak shock earlier. The SEP event was dispersive, with higher energy ions arriving before the lower energy ones. Timing suggests the particles originated at the CME when it was at $\sim 7.4 R_{\odot}$. SEP intensities increased gradually from their onset over a few hours, reaching a peak, and then decreased gradually before the CME arrived at *PSP*. The event was weak, having a very soft energy spectrum (−4 to −5 spectral index). The earliest arriving particles were anisotropic, moving outward from the Sun, but later, the distribution was observed to be more isotropic. We present numerical solutions of the Parker transport equation for the transport of 30–300 keV n^{-1} ions assuming a source comoving with the CME. Our model agrees well with the observations. The SEP event is consistent with ion acceleration at a weak shock driven briefly by the CME close to the Sun, which later dissipated before arriving at *PSP*, followed by the transport of ions in the interplanetary magnetic field.

Unified Astronomy Thesaurus concepts: Solar energetic particles (1491); Interplanetary particle acceleration (826); Interplanetary shocks (829)

1. Introduction

Solar flares and coronal mass ejections (CMEs) are known to produce significant enhancements of high-energy charged nuclei (see reviews by Kahler 1992; Reames 1999; Desai & Giacalone 2016). The largest and most intense solar energetic particle (SEP) events are associated with CMEs (Kahler et al. 1978, 1984; Gosling 1993). In these events, the nuclei are accelerated by a collisionless shock wave, driven by the CME, continuously from the time the CME erupts from the Sun, until and beyond its passage at 1 au. For fast CMEs, the shock crosses 1 au, and there is almost always a large increase in low-energy (<a few MeV) SEPs at the same time it crosses (e.g., Bryant et al. 1962; Rao et al. 1967; Reames 1999; Giacalone 2012). The enhancement at the shock is known as an energetic-storm particle (ESP) event. At higher energies (>10 MeV), the peak intensity usually occurs well before the shock arrival, and the intensity is decreasing by the time the CME is observed. This suggests that the shock accelerated the particles very rapidly near the Sun, but the acceleration rate decreased as the shock moved outward, with little additional acceleration occurring at the time the shock arrives at 1 au.

SEP events have been classified historically as either "impulsive" or "gradual," each having distinctly different properties. Impulsive events are generally related to solar flares, often less intense and shorter lived than gradual events. They are typically electron rich, have enhancements in 3He/4He up to 1000 times greater than the coronal value, and have high charge states of heavy ions (see review by Reames 1999). Gradual events are more intense and last longer. They are associated with CMEs and CME-driven shocks, as discussed above, with a composition similar to that of the solar corona (see Gosling 1993; Mason et al. 1995; Desai & Giacalone 2016).

It is widely accepted that the acceleration mechanism involved in producing CME-related SEP events is diffusive shock acceleration (DSA). The theoretical underpinnings

involved in this mechanism were developed by Krymsky (1977), Axford et al. (1977), Bell (1978), Blandford & Ostriker (1978), and Jokipii (1982). Spacecraft observations of interplanetary shocks, whether related to CMEs, corotating interaction regions, or transient disturbances, are often associated with enhancements of high-energy particles (e.g., Barnes & Simpson 1976; McDonald et al. 1976; Gosling et al. 1981; Scholer et al. 1983; van Nes et al. 1984; Gloeckler et al. 1985; Kennel et al. 1986; Beeck & Sanderson 1989; Tan et al. 1989; Lario et al. 2003; Giacalone 2012, and references therein). This mechanism has also been generalized to nonshock gradual plasma compressions (Giacalone et al. 2002, 2005).

Parker Solar Probe (*PSP*) (Fox et al. 2016) was launched in 2018 August and has since ventured closer to the Sun than any prior space probe. In addition to observations of the solar wind, solar magnetic field, and corona, it provides measurements of SEPs using the IS⊙IS instrument suite (McComas et al. 2016). Initial observations from the first two perihelia are presented in Bale et al. (2019), Howard et al. (2019), Kasper et al. (2019), and McComas et al. (2019). McComas et al. analyzed an SEP event that was observed to begin on day of year (DOY) 315, 2018, associated with a CME that erupted from the Sun late on DOY 314 and was observed by *PSP* on DOY 316. It is the purpose of this paper to provide a deeper analysis of this SEP event and to present new numerical modeling of the transport of the particles from the CME to *PSP* in order to derive diffusion coefficients and properties of the source.

2. Instrumentation

EPI-Lo is an energetic ion sensor that measures ion energy and composition and samples over 2π steradians (McComas et al. 2016; Hill et al. 2017). EPI-Lo measures the angular distribution of ions with better than 22.°5 resolution; the angular coverage for each look direction is shown in Figure 2 of Hill et al. (2017; see also Hill et al. 2020), including obscurations imposed by various structures on *PSP*. EPI-Lo can also determine ion mass with sufficient mass resolution to separately characterize H, 3He, 4He, O, and Fe over an energy range of 50 keV–2 MeV for protons and 160 keV to >10 MeV for oxygen, as well as separating 3He and 4He between 0.12 and 6 MeV. However, in this paper we use only the IonTOF data product, which records the ion time of flight (TOF) in the instrument but does not record ion energy. This product sorts the ion events by look direction and velocity but does not discriminate according to mass. The advantage is that for low-intensity SEPs, this product has higher efficiency, and achieves better statistics and lower energy threshold, than the TOF x E products that use TOF and energy (E) to determine ion mass (at the expense of higher minimum energy threshold and lower efficiency than the IonTOF product). The IonTOF product is assigned energy and efficiency under the assumption that it is dominated by protons, an assumption usually, although not always, well justified. In the case of this CME-associated event, the IonTOF product is likely predominantly protons, but with a significant contribution from 4He, as discussed further in Section 3.1.

For the event studied in this paper, the time cadence of each measurement throughout most of the event is 8 minutes, increasing to 30 minutes very late in the event, at about the time the CME crossed *PSP*, with 14 energy bins covering the energy range 30.53–278.9 keV n^{-1}.

It is important to note that the ion intensities reported in this paper are based on a preliminary calibration that is adequate for the current study but will likely be updated as in-flight calibration provides additional constraints on the instrument's measurement characteristics.

3. Overview of the SEP Event and CME

Figure 1 is a multipanel plot showing a number of observed quantities over a 3-day period in late 2018 November. Panel (a) is the heliocentric distance of the CME observed by the *STEREO-A*/COR 2 coronograph as a function of time, which is discussed further in Section 3.2. Panels (b) and (c) show the solar wind density and radial speed at *PSP* from the SWEAP/SPC instrument (Kasper et al. 2016). Panel (d) is the magnetic field vector from the FIELDS instrument (Bale et al. 2016), with components indicated at the right of the panel and magnitude in black. Panel (e) is the flux of energetic ions from the IS⊙IS/EPI-Lo instrument with energies indicated at the right, and panel (f) is a color spectrogram showing all the data (~30–300 keV n^{-1} ions) from EPI-Lo during this event. The axis bar at the top of the figure shows the position of *PSP* relative to the Sun center. *PSP* moves approximately $5R_{\odot}$ in heliocentric distance during the SEP event.

The SEP event is characterized by a distinctive velocity dispersion feature, starting early on DOY 315, as was shown in McComas et al. (2019). Particles with energies above 100 keV arrive well before the lower energy ones, particularly those below about 50 keV. The onset of >100 keV n^{-1} ions occurs about 2:00 UT on 2018–315 (year–DOY), which is 4–6 hr after the eruption of a CME, whose position is indicated in the top panel. From inspection of panel (e), the rise from the background to the peak occurs over a few hours, depending on the energy. The spacing of the time tick marks is 2 hr in this figure; thus, at energies below 50 keV, the rise to maximum occurs over about 9 hr, whereas the rise to maximum for energies above 100 keV is about 2–3 hr. The peak intensity at all energies occurs well before the arrival of the CME at *PSP* early on DOY 316, as seen as the large increase in the magnetic field magnitude. The intensity at all energies was declining as the CME crossed *PSP* and dropped markedly at the time of the arrival of the CME at *PSP*. We note that there is an apparent feature visible in panel (f) occurring late in the day of 315 at about the same time the time resolution changes from 4 minutes to 30 minutes. This feature is an artefact of the change in time resolution and is not conspicuous in the fluxes plotted in panel (e). Mitchell et al. (2020) show a similar plot to Figure 1(f), with a uniform time resolution that does not reveal this feature.

Energy spectra for three time intervals are shown in Figure 2. The black symbols represent the average over all of DOY 315, which covers most of the event. A power-law least-squares fit to the event-averaged spectrum gives a spectral index of −4.7. In another paper in this volume, Desai et al. (2020) analyze energy spectra for this and other events seen by IS⊙IS, finding that the event-averaged 4He spectrum for this event is significantly harder with an approximately −3 spectral slope. As mentioned in Section 2, our analysis is based on a preliminary calibration, which is suitable for this study but also leads to some uncertainty in the precise spectral slope of this event. We are confident it is in the range −4 to −5. This is differential intensity versus kinetic energy. Converted to phase-space density versus momentum, this would correspond to a spectral index in the range of −10 to −12. This is a remarkably

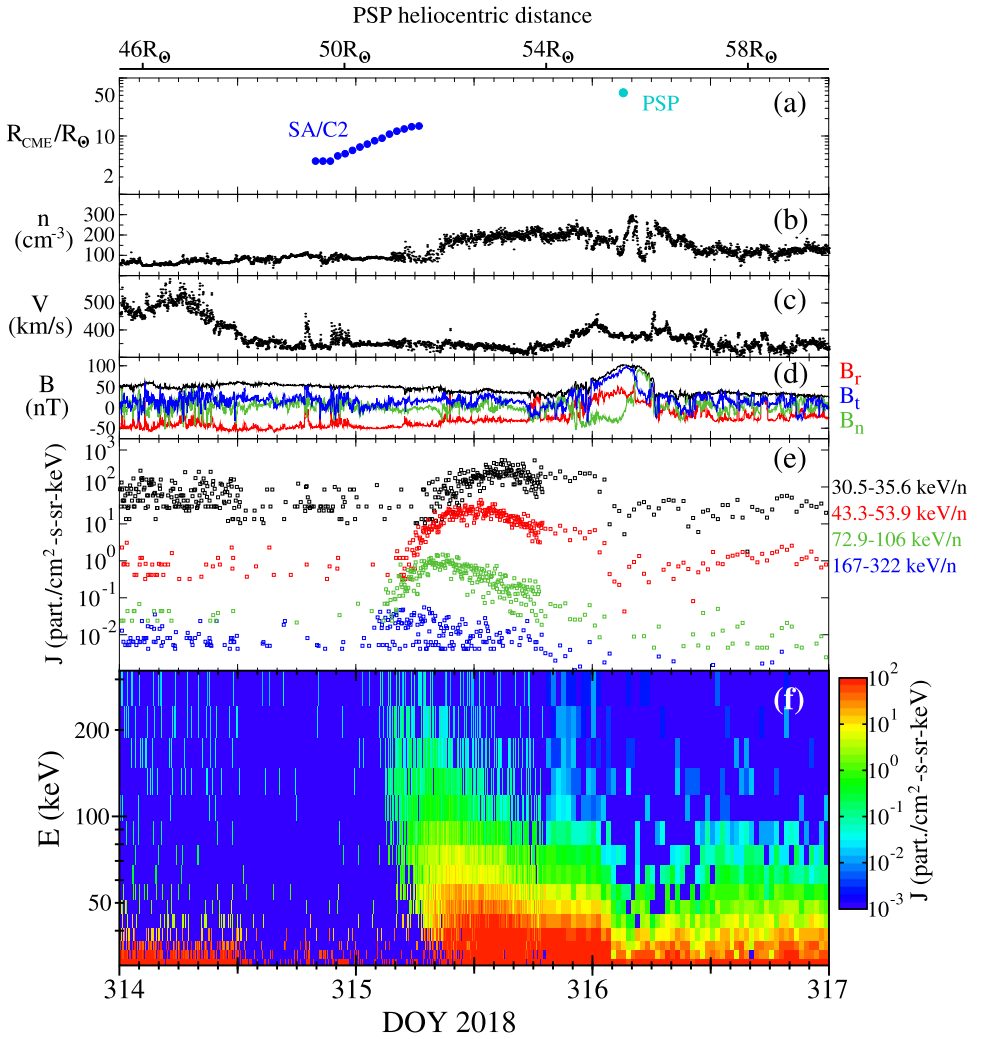

Figure 1. Overview of the SEP event. (a) The heliocentric distance of the CME observed by *STEREO-A*/COR2 (blue solid circles) and by *PSP* (cyan solid circle); (b) and (c) the solar wind density and radial component of the velocity, respectively; (d) the magnetic field vector and magnitude, with components indicated at the right of the figure; (e) the flux of energetic ions, with energies indicated at the right; and (f) a color-coded energy versus time diagram with the color indicating the flux. The upper axis bar shows the position of *PSP* during this time interval. See the text for additional details.

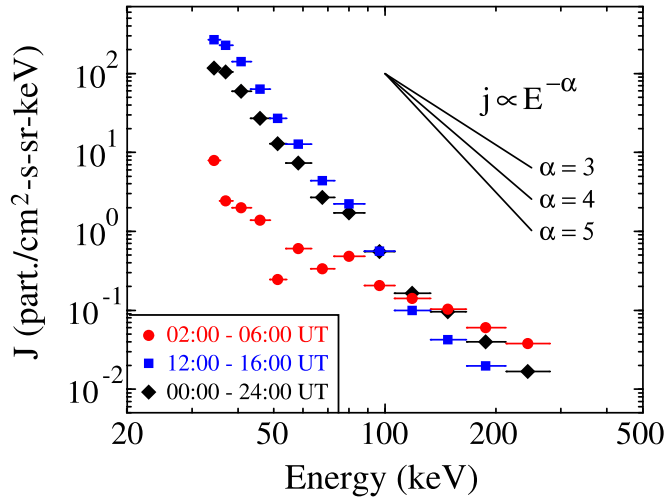

Figure 2. Energy spectra during 2018–315. Red symbols are averages over the period 2:00–6:00 UT, blue are averages over 12:00–16:00 UT, and black is averaged over the entire day.

steep spectrum and indicative of a very weak event. Earlier in the event the spectrum is harder, as shown with the red symbols, and it is a bit softer later in the event. The four lowest energy points in the spectrum during the early part of the event, in red, are not likely associated with the event, as can be seen by inspection of Figure 1(f). These fluxes are part of the background, having very few counts, whose statistical properties are studied by Bandyopadhyay et al. (2020). Thus, during the early phase of the event, low-energy "event-associated" particles are likely absent.

Although no obvious shock was observed by *PSP* during this event, it is possible that the CME drove a shock briefly as it was closer to the Sun (see McComas et al. 2019). This is discussed more in the next section. The observed spectrum can be used to constrain the density compression across such a shock, if one ever existed, by invoking the theory of DSA (Axford et al. 1977; Krymsky 1977; Bell 1978; Blandford & Ostriker 1978; Jokipii 1982). In this theory, the phase-space density, $f_{\rm DSA}$, at the shock has a power-law dependence on the particle momentum with an index of $-3s/(s-1)$, where s is

the density compression across the shock. This power-law index would result at the shock, at high energies, even if the spectrum of the source of particles were also power law with a larger spectral index (softer spectrum) than this. To obtain a phase-space density with a -10 power-law dependence on momentum the density compression would be $\sim$1.4. If the shock normal is parallel to the incident magnetic field, this would be associated with a sonic Mach number of about 1.3. This is a very weak shock. There is some uncertainty in this constraint since the theory only gives the spectrum at the shock, which was not observed locally. If the shock ever existed, when it was closer to the Sun, the spectrum there would likely differ from the event-averaged fluence spectrum that we observe locally, depending on the transport parameters of the particles. This is discussed further in Section 5. We also note that shocks are *not* a requirement for particle acceleration since nonshock plasma compressions are also capable of accelerating particles (e.g., Giacalone et al. 2002) in a manner that is essentially the same as DSA.

3.1. SEP Composition

EPI-Lo also detected 4He for this event, at intensities roughly 4% of the proton intensities at the same energy per nucleon (Desai et al. 2020). No 3He above background was detected. We estimate that the 3He/4He ratio is well below 1% for this event. EPI-Lo also detected oxygen and iron. These are not calibrated well enough to provide reliable abundances. For the remainder of this paper, we assume the event is dominated by protons.

EPI-Lo did not detect electrons above the instrument background. There were approximately $\sim$40,000 electron detections per day over the 35–425 keV energy range, uniformly distributed over each day, with no discernible feature associated with this event. It is important to note that the EPI-Lo electron detection is a single parameter measurement—the energy deposited in a single solid state detector—therefore, the background levels are much higher than they are for the ions. In contrast, there were about 2000 ion counts for this event with energies above 100 keV n^{-1}. Its is perhaps not surprising we saw no electron signal given that this is a very weak SEP event. Cliver (2016) used the e/p ratio to compare fluxes of $>$100 MeV protons to 0.5 MeV electrons, considerably higher than what was observed for this event, finding a clear distinction between flare-associated and CME shock–associated events. Unfortunately, we are unable to use the e/p ratio as a constraint in this case given the high electron background and weak nature of this event.

3.2. The CME of 2018 November 10–12

No CME was identified in SoHO/LASCO images at this time because *PSP* was in opposition with the Earth. *PSP* was, however, located at quadrature with *STEREO-A* (STA) such that the CME observed by the COR-2 (C2) instrument on STA was roughly propagating in the direction of *PSP*. STA/C2 observed the eruption of a CME at $3R_{\odot}$ off the east limb of the Sun (from the perspective of STA/C2) near 18:00 UT on 2018–314 (2018 November 10).

We have analyzed a series of images from the STA/C2 coronagraph. Assuming the CME is in the plane of the sky of STA/C2, we computed the distance between the CME and the center of the Sun as a function of time. This is shown with blue symbols in Figure 1(a). The CME was measured in situ by the FIELDS instrument on *PSP* on November 12 (see Bale et al. 2019; McComas et al. 2019). The cyan solid circle symbol in the top panel represents the CME location at *PSP*. We estimate the speed of the CME by fitting the CME position versus time to a line starting at about 02:00 UT on DOY 315 (November 11), when the CME was about $7.4R_{\odot}$ from the Sun, assuming it moves with constant speed. This gives an average propagation speed of 360 km s^{-1}. Prior to 02:00 UT, when the CME was below $7.4R_{\odot}$, it was moving slower. But at 02:00 UT it began to accelerate, moving faster throughout the remainder of the time it was within the field of view of STA/C2 (McComas et al. 2019). A more detailed analysis of the evolution of the CME and its in situ signature is given elsewhere in this volume (e.g., Nieves-Chinchilla et al. 2020). Our estimate of the CME speed is consistent with these analyses.

The central axis of the CME (i.e., the CME nose) was roughly propagating along a Carrington longitude of 355° and $-1°$ in latitude. The latitudinal extent of the CME based on a simple analysis of the STA/C2 images is about 10°–20°. The longitudinal extent of the CME is certainly greater than its latitudinal extent. Using the CME reconstruction of Rouillard et al. (2020) and assuming that the flux rope was horizontal (east–west oriented), a successful interpretation of its aspect both in STA/C2 images and in situ could be achieved (see McComas et al. 2019). The CME reconstruction of interest here gives an angular separation between the eastern and western flank of about 85° at 06:00 UT on DOY 315. The reconstruction technique assumes a circular current channel for the flux rope, which may be an overestimate of the longitudinal extent of the actual CME in this study. Unfortunately, a frontal view of the CME is lacking to constrain the longitudinal extent better. For this reason, we focus in this study on the derived CME properties close to the imaged apex of the CME since the actual shape of the flux rope away from the apex region is subject to considerable uncertainty.

For the duration of the SEP event on DOY 315, *PSP* moved about 5° in heliocentric longitude, from 331°.2 to 325°.8 Carrington longitude. Assuming that the CME moved almost directly toward *PSP*, this suggests that the magnetic field lines associated with the magnetic field measured in situ by *PSP* all connect to the CME throughout the duration of the SEP event. In Figure 3 we use the CME 3D reconstruction model presented in Rouillard et al. (2020) and applied to the present CME (McComas et al. 2019) to determine the CME position and extent in 3D. The *PSP* orbit is shown at 04:08 UT on DOY 315. We also present in this figure the field lines associated with the Parker spiral magnetic field that connect *PSP* to the surface of the flux rope by assuming that the speed of the background solar wind upstream of the CME was 350 km s^{-1}. The locus of all the field lines that connect the portion of the *PSP* orbit during the time interval of CME propagation from the corona to *PSP* is also shown. Figure 3(a) shows that the magnetic connection with the CME is established early in the event, and some $\sim$14° eastward of the reconstructed CME nose. In Figure 3(a) we also overplot along the CME surface the CME speed determined by the 3D reconstruction. For the region that is magnetically connected to *PSP* we find a maximum speed of $\sim$380 km s^{-1}.

Further modeling of this CME with the methods presented in Kouloumvakos et al. (2019) shows that there is no obvious CME shock connected to *PSP* throughout the CME

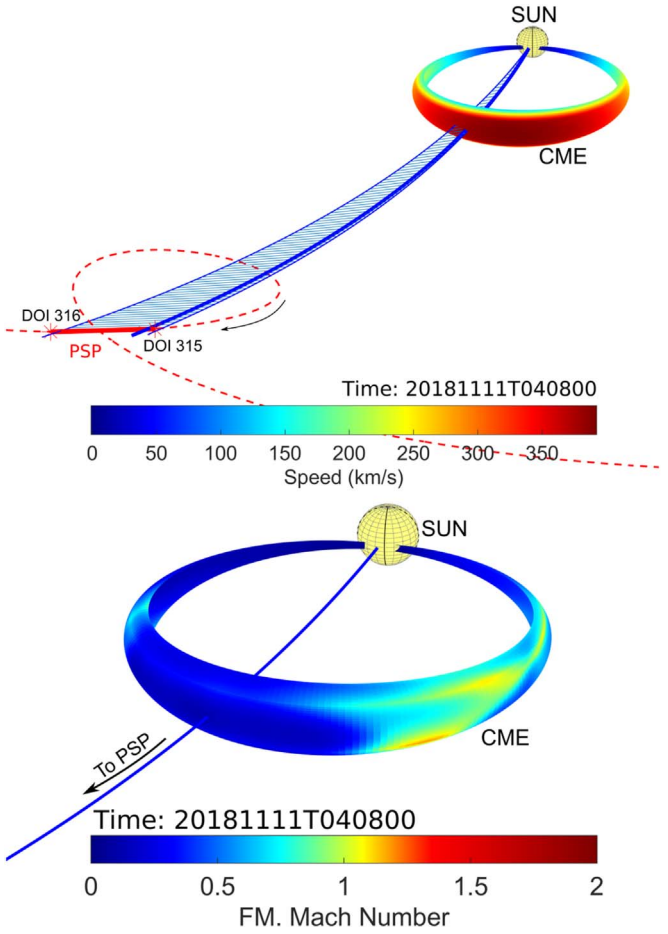

Figure 3. 3D view of the reconstructed CME and the distributions of the modeled shock parameters over the CME surface for 2018 November 11 at 04:08 UT. Top panel: 3D distribution of the CME speed over the reconstructed CME flux rope. The blue shaded area depicts the locus of Parker spirals connecting *PSP* to the flux rope, and the red thick line, the orbit of *PSP* during the first encounter. Bottom panel: A focused view of the 3D distribution of the fast magnetosonic (FM) Mach number over the CME surface.

propagation, assuming the magnetic field is a simple Parker spiral. The technique assumes that if a shock occurred, it developed at the surface of the flux rope. It then computes the fast magnetosonic (FM) Mach number and the density compression ratio (X) by exploiting the 3D speed at the surface of the flux rope as well as the background solar wind upstream of the event. The background coronal/solar wind model used here is the magnetohydrodynamic around a sphere thermodynamic (MAST) model developed and provided by Predictive Sciences (Lionello et al. 2009; Riley et al. 2011). Figure 3(b) presents a prediction of the FM Mach number over the CME surface, at 2018 November 11, 04:08 UT. At that time the solar wind at the CME surface varied from ∼220 to 340 km s^{-1} and the fast mode speed varied from ∼160 to 380 km s^{-1}, from the CME flanks to the nose. The FM Mach number and X are less than unity over most of the CME surface, suggesting there is no shock. This is also confirmed by the lack of a CME shock measured in situ at the time of CME passage at *PSP*. However, there is evidence that a region with FM Mach <2, and $X > 1$ could have developed a shock over an extended region near the western flank of the CME. In this region a subcritical quasi-perpendicular shock may have formed. Given the interplanetary magnetic field is turbulent, the magnetic field lines wander in space (e.g., Jokipii & Parker 1969), with a characteristic angular scale that is similar to that associated with solar supergranulation (Giacalone & Jokipii 2004), which is about ∼10°. Because this is a turbulent, random walk process, some field lines meander well beyond the characteristic scale. Thus, it is reasonable to expect that *PSP* crossed through magnetic field lines that also connect to the western flank of the CME. We note that Pei et al. (2006) studied the effect of this field-line random walk on the onset times of SEP events at Earth. Using the results presented in their study, and assuming nominal values for the level of interplanetary magnetic-field turbulence (see Figure 4 of their paper, open circle symbols compared with straight black line), we estimate that the field-line random walk adds less than ∼5% to the field-line path length compared with the case without turbulence.

3.3. SEP Anisotropies

Figure 4 shows the anisotropies for the SEP event along with the color-coded flux energy versus time diagram in a similar format as Figure 1(f), but only for DOY 315. The regions indicated with the solid white lines in the bottom panel show the time intervals and energy ranges over which the anisotropies are plotted in the upper panels. The energy range is also indicated above each anisotropy plot. The color in each of the anisotropy plots is a representation of the flux, in units of cm^{-2} s^{-1} sr^{-1} keV^{-1}, with red being the largest value and blue the smallest value. Black is zero, and the gray background represents no measurements. The range of colors for each anisotropy plot differs from that shown in the bottom panel, and they also differ from each other. The range of values are provided in the legend above each plot.

The anisotropy plots show the measurements made by the array of sensors indicated in Figure 2 of Hill et al. (2017). In Hill et al. (2020), a revised version of the instrument-array figure appears where the azimuth and elevation angles are given. The direction of the Sun is toward the upper left of each of the anisotropy plots. The direction of the magnetic field, averaged over each of the time intervals, is indicated with a black arrow and "B" symbol in Figure 4. This was determined by analyzing the magnetic field in spacecraft coordinates, averaged over each time interval, the location of each detector in the array in spacecraft coordinates, and the boresight direction of each detector. We also show dashed lines that place these detectors in two of the eight different sectors, the ones directed toward and opposite the Sun. The sectors are numbered in the same manner as in Hill et al. (2020) such that sector 3 is the sunward sector and sector 7 is opposite to this. These are used to estimate the anisotropy in the plasma frame discussed below.

For the earliest time interval shown from 2:00 to 3:00 UT in the upper left anisotropy plot, only the sunward-directed sensors observe particles. Thus, the earliest arriving particles, with energies above 100 keV, are moving antisunward. From inspection of Figure 1(d), the magnetic field during this time is dominated by the radial component. This suggests that the earliest arriving particles are moving radially away from the Sun with little pitch-angle scattering in the interplanetary field.

The earliest arriving low-energy ions, at about ∼30–100 keV, represented by the second anisotropy plot from the left during 7:00–8:00 UT, are also generally moving antisunward, but there are considerably more sensors with counts. This suggests that these ions have undergone some scattering

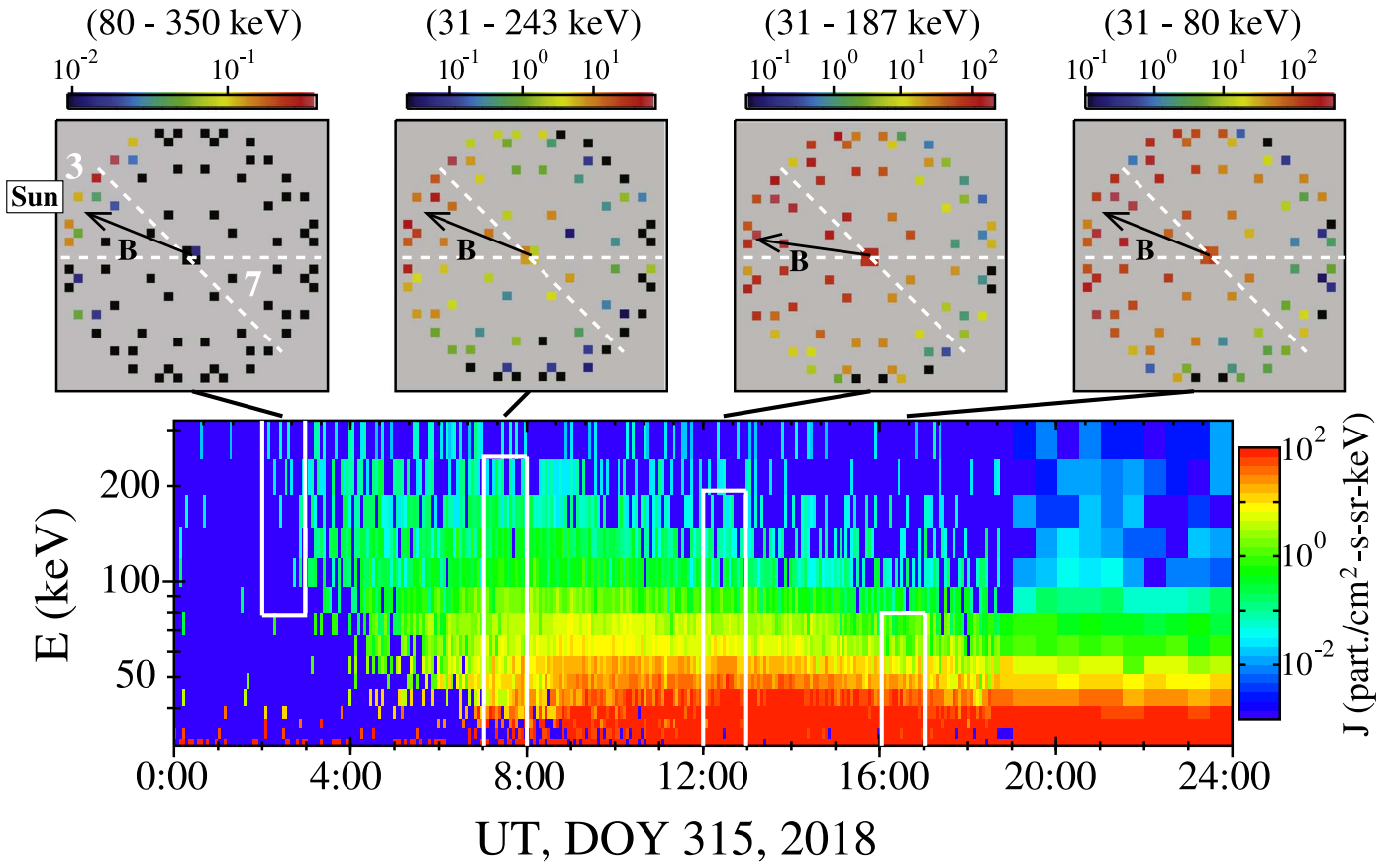

Figure 4. Top plots: fluxes of ions over the energy range indicated at the top of each plot, observed in each of the EPI-Lo sectors indicated with small squares arranged within a circle. The time intervals over which the anisotropies are determined is shown with the white lines in the bottom plot. The gray box is the plot background, and there are no measurements in this region. Each plot has a different range of fluxes represented with a color, with a range indicated by the legend above each plot. The units are the same as in the lower plot. The arrow and "B" symbol represent the direction of the magnetic field vector averaged over the time interval. The white dashed lines indicate two sectors of the instrument, with sector 3 toward the Sun and sector 7 away from the Sun, as indicated in the left-most plot. Bottom plot: color spectogram of the flux ion flux for DOY 315, 2018, in a format that is similar to that in Figure 1(f).

during their transit from the source. Later in the event, as can be seen by the two upper right anisotropy plots, nearly all of the EPI-Lo sensors have counts, although there are more in the sunward-directed hemisphere (i.e., the particles are moving antisunward). These are dominated by low-energy ions, below about 80 keV. Ions with these energies are moving slowly enough that advection with the solar wind leads to an anisotropy in the spacecraft frame of reference.

Using the counts in the different sectors we can estimate the anisotropy in the plasma frame by adjusting for the Compton–Getting effect (e.g., Gleeson & Axford 1968). The total flux of ~31–73 keV ions in sector 3, the sunward-directed sensors, for the period 12:00 UT–13:00 UT is ~1700 cm^{-2} s^{-1}, sr^{-1} keV^{-1} and in sector 7, containing the antisunward sensors, it is ~55 cm^{-2} s^{-1}, sr^{-1} keV^{-1}. This gives a front-to-back flux ratio, in the spacecraft frame of reference, of about 30. Using a simple linear Compton–Getting correction, we can estimate the fluxes in each of these sectors in the local solar wind frame. The linear Compton–Getting correction is $J' = J[1 - 2(\gamma + 1)(U/v)\cos\alpha]$, where J' and J are the fluxes in the solar wind and s/c frames, respectively, γ is the (assumed) power-law exponent of the flux versus energy, U is the solar wind speed, v is the particle speed, and α is the angle between the solar wind velocity vector and the instrument plane. Taking, for sectors 3 and 7, $\alpha = 40°$ and $\alpha = 140°$, respectively, $U = 345\,km\,s^{-1}$ (the average solar wind speed over this time interval), and $v = 3 \times 10^8\,cm\,s^{-1}$ (speed of a 47 keV proton, the logarithmic midpoint of the energy range), we find that the plasma-frame fluxes in sectors 3 and 7 are approximately equal for the case of $\gamma = 4.3$. This is close to the event-averaged energy spectrum discussed in Section 3. A similar result is obtained for the last time interval (16:00–17:00 UT). This suggests that the measured distributions later in the event, after the initial rise, are approximately consistent with the advection of an isotropic distribution in the local plasma frame that passed the spacecraft. This indicates there is considerable scattering of these ions in the interplanetary field. We emphasize, however, that this is an initial calculation of the Compton–Getting correction. As noted previously, there is some uncertainty in the measured spectrum since we have only performed an initial calibration of the instrument. Moreover, for such low particle speeds and steep energy spectra, the Compton–Getting correction is quite large. A more accurate correction should include higher order, nonlinear terms.

4. Event Onset Time Analysis

Figure 5 shows the time of the event onset as a function of energy. For each energy band, the flux was plotted versus time and the time of the event onset was determined by eye, using rather conservative error estimates. The horizontal error bars in this figure represent a range of times over which the event

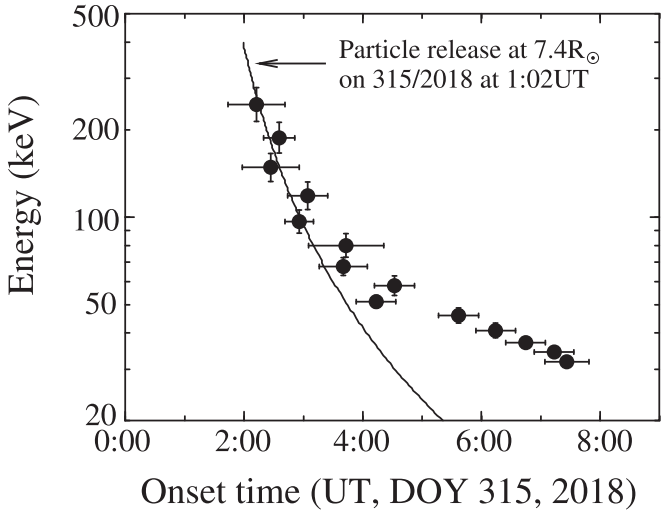

Figure 5. The time of the event onset at each energy. The black curve is the theoretical expectation assuming the particles were released from the CME at the position and time indicated and propagated radially to *PSP* without scattering (ballistic propagation). See the text for additional details.

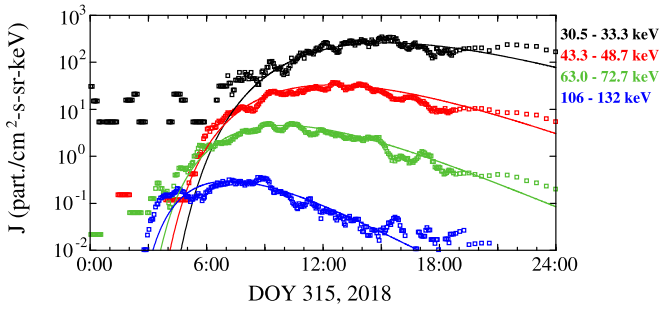

Figure 6. The symbols show the ion flux measured by EPI-Lo vs. time for the energies indicated. The curves show the results from our calculation of the Parker transport equation. The source starts at $7.4R_\odot$ with a power-law dependence on momentum. The source moves outward with the CME at 360 km s^{-1}, but the intensity decays with time over about 3 hr, with the intensity of higher energy ions decreasing sooner than that of the lower energy ions. See the text for additional details.

could have reasonably started given the uncertainty associated with the background. At times to the left of the left-most extent of the error bar, the event clearly had not yet started, while for times greater than the right-most extent of the error bar, the event was clearly in progress. The onset time is not an easily defined quantity due to the significant variability in the fluxes. Regardless, it is clear that the onset time has a significant dependence on energy, and this plot also clearly reveals the distinctive velocity dispersion feature visible in Figure 1(f).

Assuming the particles move radially outward, which is reasonable given the discussion of the anisotropies in the previous section, if a 300 keV proton (speed = 7580 km s^{-1}) originated at the Sun it would take 1.28 hr to arrive to *PSP*.[18] Thus, if the source were at the solar surface, these particles would have been released at about 0:40 UT on DOY 315. At this time, the CME had already erupted and was moving outward toward *PSP*. Moreover, the angular extent of the CME is about 10°–20° based on images from STA/C2, which is larger than the 5° change in heliolongitude of *PSP* during 2018–315. Thus, had these particles been released at the Sun, they would have had to pass through or around the CME in order to arrive to *PSP*, which would be challenging to model given the complex magnetic topology involved. We suggest, instead, that the particles originated at the CME itself, or just in front of it at a weak shock or plasma compression. We note that interplanetary field-line random walk, which might facilitate the magnetic connection of *PSP* to the western portion of the CME where a shock could have formed, increases the path length of the particles compared with the case of purely radial transport. However, as noted at the end of Section 3.2, it is not likely that this significantly alters the arrival time of the particles at *PSP*.

The black curve in Figure 5 represents the arrival time of protons as a function of energy assuming the particles are released from the CME when it was at $7.4R_\odot$ at 1:03 UT on DOY 315. We note that this curve passes through the onset times of the highest energy particles, above 100 keV, but not the lower energy ones. The onset time of the lower energy particles is significantly later, which is likely the result of instrument sensitivity, as discussed further below.

As noted in Figure 4, the earliest arriving particles are observed to be coming from the Sun with a significant anisotropy, and the magnetic field was observed to be nearly radial during the first few hours of DOY 315 when the CME—the source of the particles—was moving away from the Sun. Thus, we can estimate the path length of the ions by assuming scatter-free, radial propagation. The path length is simply $d = v(t_{\rm onset} - t_0)$, where $t_0 = 315.043$ days is the time of the particle release, $t_{\rm onset}$ is the onset time plotted in Figure 5, and v is the particle speed. From this, we find that the path length of ions with energies above 100 keV is approximately 0.21 au, which is about $45R_\odot$. In contrast, the path length of ions with energies lower than 50 keV is 0.32–0.38 au, ($\sim$70–80$R_\odot$), almost twice that of the higher energy ions.

Assuming the CME is the source of all the energetic particles associated with this SEP event, it is clear the lower energy particles take a much longer total path to arrive at *PSP*. One possibility is that the lower energy ions follow magnetic field lines, which meander in space on a spatial scale larger than the gyroradii of the lower energy ions, but shorter than the higher energy ions, possibly related to the magnetic "switchbacks" discussed by Kasper et al. (2019) and Bale et al. (2019). Because the difference in the gyroradius of a 100 keV proton and a $\sim$30 keV proton is only about a factor of 1.8, we find this unlikely. This is discussed further in Hill et al. (2020).

Another possibility is that the lower energy ions are more efficiently scattered in the interplanetary magnetic field so that their transport to *PSP* is delayed. The anisotropies shown in Figure 4 show evidence of this as there is a smaller anisotropy for the first-arriving lower energy ions than the higher energy ions, as seen by comparing the upper two left panels. The lack of scatter-free low-energy ions is likely the result of instrument sensitivity. Note from Figure 5 that scatter-free 30 keV protons should arrive to *PSP* at about 4:30 UT. By inspection of Figure 6 (see also Figure 1(e)), particles with this energy associated with the event are likely below the background.

As we show below, the fluxes of the ions observed for this event can be fit with a diffusive transport model, suggesting that the delay in the arrival of low-energy ions is the result of scattering in the interplanetary medium. Another interpretation

[18] This neglects the speed of the spacecraft, which, on DOY 315, 2018, was $\sim$38 km s^{-1}, about 200 times less than the speed of a 300 keV proton.

of the delay of the low-energy ions is discussed in Mitchell et al. (2020) and at the end of Section 6 below.

5. A Model for the Diffusive Transport of the SEPs

The time variation in the SEP fluxes shown in Figures 1(e) and (f) and the anisotropies at all but the highest energies shown in Figure 4, and discussed in Section 3.3, are suggestive of diffusive transport of these ions. While there is some uncertainty in the observed spectrum and the use of a linear Compton–Getting correction to convert the anisotropies to the plasma frame, our initial calculation suggests that the distributions are approximately consistent with isotropy in the solar wind frame. Thus, as an initial approach to modeling this event, it is reasonable to fit the flux profiles to solutions of the Parker transport equation (Parker 1965), which is valid when the particles' pitch-angle distributions are nearly isotropic.[19] By fitting these solutions to the observed fluxes, we obtain diffusion coefficients and properties of the source.

The Parker equation contains all of the major charged-particle transport effects such as spatial diffusion in turbulent magnetic field fluctuations, advection with the solar wind, drifts in the large-scale magnetic field, and energy change resulting from particle transport through plasma compressions or rarefactions. There is no pitch-angle information contained in the equation since it assumes quasi-isotropy. It is also averaged over gyrophase. The resulting distribution function depends only on the magnitude of the particle momentum, position, and time.

For simplicity, we consider a spherically symmetric geometry. The distribution function of energetic particles, f, the particle diffusion coefficient, κ, the plasma flow speed, U, and the source of low-energy particles, Q, depend only on one spatial coordinate, r, the distance measured from the center of the Sun. During the SEP event, prior to the arrival of the magnetic flux rope associated with the CME, the magnetic field was observed to be nearly radial. Moreover, *PSP* moved only about 5° in solar longitude during this period, which is less than the 10°–20° angular extent of the CME inferred from the STA/C2 observations and modeling, as discussed above. Thus, a spherical geometry is reasonable. Under these simplifying assumptions, Parker's transport equation becomes

$$\frac{\partial f}{\partial t} - \frac{1}{r^2}\frac{\partial}{\partial r}\left(r^2\kappa\frac{\partial f}{\partial r}\right) + U\frac{\partial f}{\partial r} - \frac{1}{3r^2}\frac{\partial (r^2U)}{\partial r}\frac{\partial f}{\partial \ln p} - Q = 0, \quad (1)$$

where p is the magnitude of the particle momentum and t is time.

We use the same model as described in Giacalone (2015), who studied SEP acceleration at fast interplanetary shocks, except that in this case we neglect the shock and take the bulk solar wind speed to be constant. The diffusion coefficient is assumed to be proportional to r^2, which is consistent with it scaling inversely with the magnetic field strength since the field is approximately radial during this event. The source function is chosen to be representative of particles accelerated at a very weak shock, or compression, associated with the CME, which lasts for a few hours. It is given by

$$Q(r, p, t) = A\delta(r - r_{\rm CME}(t))p^{-9}e^{-t/\tau(p)}, \quad (2)$$

where $R_{\rm CME}(t) = 7.4R_\odot + V_{\rm CME}(t - t_0)$, $\tau(p)$ is the momentum dependent decay time, discussed below, and A is a normalization constant. The speed of the CME is taken to be 360 km s^{-1}, as observed (see Section 3.2), and t_0 is the time at which the CME first began to accelerate particles, taken to be decimal day 315.043 (November 11, 1:02 UT). Of course, it takes time to accelerate particles, and the acceleration time is assumed to be shorter than the duration of the source. This is discussed further in the next section. The assumed power-law exponent of the momentum dependence of Q is chosen to be a bit harder than the observed event-averaged spectrum as discussed in Section 3 and gives the best fit to the data (see below).

The decay time, $\tau(p)$, appearing in Equation (2) represents the time duration of the source. It is not possible to fit the data to an impulsive injection at all energies. It is physically reasonable that the source is a function of time since the CME likely accelerated particles continuously for a certain time interval before it weakened, with a duration that depends on energy. We use the following form for the decay time:

$$\tau(p) = 2.75\left(\frac{E}{31.9{\rm keV}}\right)^{-0.5}{\rm hr}, \quad (3)$$

where E is kinetic energy. The physical interpretation is that the source is a very weak shock or plasma compression that accelerates particles with a power law (the −11 exponent in Equation (2)) only for a short time, and in a manner that depends on energy. Note that a shock is not strictly required for particle acceleration (e.g., Giacalone et al. 2002), which is discussed more below. The acceleration rate decreases with time, as the shock/compression weakens. As the acceleration rate decreases, the number of high-energy source particles also decreases. Thus, the source of higher energy particles will decrease more rapidly than the lower energy ions. After a few hours, the source is very weak and no longer contributes to the particles seen by *PSP* later.

The diffusion coefficient that gives a reasonable fit to the data is given by

$$\kappa(r, p) = \kappa(r_0, p_0)\left(\frac{r}{r_0}\right)^2\left(\frac{p}{p_0}\right)^{9/4}, \quad (4)$$

where r_0 is a reference helioscentric distance, taken to be $r_0 = 7.4R_\odot$, and p_0 is a reference momentum, taken to be that of a 10 keV proton. We find that $\kappa(r_0,\ p_0) = 2.7 \times 10^{17}$ cm^2 s^{-1} gives the best fit to the data. This is the diffusion coefficient of a 10 keV proton at $7.4R_\odot$.

Figure 6 shows the results of our model calculation compared with the observed fluxes. The observed fluxes have been smoothed using a 10-point running average. The comparison is reasonable, although not for the early part of the event. This is to be expected since the Parker equation assumes the distributions are isotropic, which is not consistent with the observations during the initial rise phase of the event.

Note that there may be other ways to represent the source and diffusion coefficient that also produce a reasonable fit to the data. The choices above, while physically motivated, are

[19] We note that the earliest part of the observed event is not isotropic, so our model applies to the time after the initial rise in the particle intensity.

Table 1
Parallel Mean-free Path and Diffusive Length Scale from Diffusive Transport Modeling and Data Comparison

Energy (keV)	r (au)	$\lambda_\parallel$ (au)	$\lambda_\parallel$ ($R_\odot$)	κ/U ($R_\odot$)
30	0.05	1.6×10^{-3}	0.35	0.8
50	″	2.3×10^{-3}	0.48	1.4
100	″	3.5×10^{-3}	0.75	3.1
30	0.25	0.041	8.8	20
50	″	0.057	12.1	36
100	″	0.087	18.7	78
30	1	0.66	141	322
50	″	0.9	194	572
100	″	1.4	300	1.25×10^3

Note. Where $U = 350$ km s^{-1} is assumed.

not necessarily unique. Moreover, extensions of the Parker equation to include pitch-angle information, such as the focused transport equation (Ruffalo 1995; Kota 2000; Droge et al. 2010; Schwadron et al. 2010), will likely yield similar results and lead to a better fit during the early part of the event.

6. Discussion

The diffusion coefficients derived in the previous section can be related to the mean-free path of scattering, parallel to the mean magnetic field, by $\lambda_\parallel = 3\kappa/v$. Using Equation (4), with $\kappa(r_0, p_0) = 2.7 \times 10^{17}$ cm^2 s^{-1}, we obtain values for the mean-free path at 0.25 au (near where *PSP* is during this time) and at 1 au for three different energies, which are tabulated in Table 1.

The values for $\lambda_\parallel$ near the orbit of *PSP* are smaller than the heliocentric distance of *PSP* at this time by a factor of 2–5, depending on the energy. The use of a diffusive transport model, which assumes there is sufficient interplanetary scattering to isotropize the pitch-angle distribution, is clearly only marginally applicable given the values of $\lambda_\parallel$ calculated.[20] The values at 1 au are larger than those tabulated for many events by Palmer (1982), suggesting weak scattering in the interplanetary medium. We have also examined the results from our model as seen by an observer at 1 au. We find that late in the event, well after the onset phase, the particle intensities are similar to, and decay with about the same rate as, those at *PSP*. This is likely due to the large mean-free path at 1 au. It is unfortunate that no Earth-based spacecraft were magnetically connected to this event since they may have observed this as a very weak event.

In Section 3 we noted that the event-averaged energy spectrum is approximately a power law with a spectral index between -4 and -5. We also noted that such a spectrum would result from DSA theory for a weak shock whose plasma density compression is about 1.4. Our discussion of the CME concludes that while such a shock is not likely to have formed, it is possible given the uncertainties in the modeling. We are unable to determine the source of the accelerated particles, either solar wind or preexisting suprathermal particles, from these initial observations. The standard canonical power-law index, γ, from DSA theory applies even if the source spectrum is also power law, provided it has a spectral index that is larger than γ (i.e., a softer preexisting particle spectrum). There is no conspicuous evidence of any preexisting suprathermal particles in the ∼12 hr preceding this event. A statistical study of select "quiet" time periods in the *PSP*/ISOIS data set has been performed by Bandyopadhyay et al. (2020).

We also note that a shock is not required for particle acceleration. Giacalone et al. (2002) showed that any plasma compression can accelerate particles provided the particles are trapped near but move through the compression. Density compressions of about 40% would produce a similar spectrum to that at a shock having a density jump of 1.4. We note from Figure 1(b) that there is a significant density compression at 9:00 UT on DOY 315, and the compression at the CME, at about 4:00 UT on DOY 316, is also very significant. Both are larger than 40%. There is no corresponding change in plasma velocity associated with the compression at 9:00 UT, however, which is the actual requirement for particle acceleration (see Giacalone et al. 2002). It is not clear whether this density compression is related to the SEP event. Regardless, a plasma compression of the order of 40% during the time when the CME was accelerating near the Sun is certainly plausible. We should note, however, the mechanism of compression acceleration requires the diffusive skin depth of the particles, κ/U, to exceed the width of the compression in order to behave in a manner similar to DSA. Table 1 gives values of the diffusive skin depth using the results of our model. For this mechanism to work, the width of the compression when it was close to the Sun must be less than about one solar radius. Although we have no way of knowing the width of such a compression, if it existed, it is reasonable to expect its thickness to be less than this given that a true shock wave would have a thickness comparable to ion inertial length, which is easily shown to be several orders of magnitude smaller than the solar radius. Thus, even had any such compression been several thousand times greater than a typical shock thickness at this distance, it would accelerate particles in a manner similar to DSA.

Based on the above, we suggest that the SEP event is the result of particle acceleration at a weak shock or compression driven by the CME during the time when the CME was moving from $7.4R_\odot$ to $15R_\odot$. Subsequent to this, the shock or compression weakened and the acceleration rate declined, producing fewer particles, especially at high energies, eventually not accelerating any particles by the time the CME arrived at *PSP*. The particles moved ahead of the source as they were transported from the source to *PSP*. The resulting dispersive nature of the event is caused by interplanetary transport. The lower energy ions were delayed relative to the higher energy ions because of increased scattering in the interplanetary field, resulting in a smaller diffusion coefficient.

The rate of acceleration can also be computed from the diffusion coefficients derived above, assuming DSA theory. As a rough estimate, the acceleration time is approximately $\tau_{ACC} \sim \kappa/U_1^2$, where $U_1 = V_{CME} - V_{SW}$ is the plasma speed in the frame moving with the CME and V_{CME} and V_{SW} are the CME and solar wind speeds, respectively (see Drury 1983; Forman & Drury 1983; Jokipii 1992). The value of κ is determined at the energy of interest. For 100 keV protons, using Equation (4), and taking $U_1 = V_{CME} - V_{SW} \approx 60$ km s^{-1}, we find $\tau_{ACC} \sim 1.1$ days. This is clearly too long to account for the production of these particles at the CME since our interpretation requires the acceleration to have lasted less than or of the order of an hour or so. Thus, in order to have

[20] Note that the Parker equation permits a diffusive streaming anisotropy, which is required to be small, but in this case, the diffusive streaming anisotropy ($=3\kappa\nabla f/(vf) = \lambda_\parallel/r$, where v is the particle speed and r the radial distance) is not particularly small, except for near the Sun.

sufficiently rapid acceleration to produce these particles in a short period of time, the diffusion coefficient would have to be substantially reduced near the shock or compression. It is important to note that gradual SEP events at Earth, especially large ones, are well known to exhibit features that suggest the transport coefficients far upstream of the CME are considerably larger than at the shock itself. In fact, in a typical gradual SEP event associated with a CME-driven shock, the SEP intensity increases gradually several hours before the arrival of the shock and then increases very rapidly right at the shock. This is associated with a much smaller diffusion coefficient near the shock (e.g., see Giacalone 2012 and references therein). The reduction in diffusion coefficient, in the case of large events and fast shocks, is thought to be the result of increased magnetic wave activity near the shock, possibly related to the back reaction of the energetic particles (Bell 1978; Lee 1983, 2005; Lee et al. 2012). We note, however, that there is no obvious evidence in the local measurements of the magnetic field of such wave activity, and given that this event is quite weak, it seems unlikely that there were sufficient intensities of energetic particles to excite strong waves closer the Sun. Another means of reducing the diffusion coefficient is by the magnetic geometry (e.g., Jokipii 1982) since the perpendicular diffusion coefficient is generally much smaller than the parallel diffusion coefficient (e.g., Giacalone & Jokipii 1999). As discussed in Section 3.2, a portion of the CME's western flank may have been a quasi-perpendicular shock, and the acceleration rate may have been considerably more rapid than our calculation above. In another paper in this volume, Schwadron et al. (2020) analyzed SEPs associated with a different CME observed by *PSP*, including the local enhancement at a nonshock plasma compression region, finding a much smaller mean-free path than we have obtained here. This analysis is for the actual site of acceleration, which is not observed in our case. Thus, the larger mean-free paths obtained in our study, shown in Table 1, are representative of that associated with the propagation away from the CME.

It is also noteworthy that the diffusion coefficient given by Equation (4) has a very strong dependence on momentum. Quasi-linear theory (Jokipii 1966) predicts that $\kappa_{QLT} \propto p^{4/3}$ for particles moving in a turbulent magnetic field with a power spectrum having a Kolmogorov-like $-5/3$ power-law dependence on wavenumber. For $\kappa \propto p^{9/4}$, as used in our fits to the data for this event, the magnetic field power spectrum, P, would have to obey $P \propto k^{-3/4}$, assuming quasi-linear theory is valid and that the characteristic scale of the fluctuations was much larger than the gyroradii of the particles. The observed magnetic switchbacks (Bale et al. 2019; Kasper et al. 2019) might have a significant effect on the resulting energy dependence of the diffusion coefficient.

7. Summary and Conclusions

We have analyzed *PSP*/IS⊙IS/EPI-Lo observations of a SEP event occurring on 2018 November 11 when the spacecraft was approximately 0.25 au from the Sun. We also solved the Parker transport equation to model the observed ion fluxes. From our analysis, we conclude the following:

1. The SEP event is most prominent in ions with kinetic energies from ∼30 to 300 keV n^{-1}. There were no energetic electrons. There was a significant fraction of 4He (∼4% at the same energy per nucleon) but no 3He. The ratio 3He/4He is well below 0.1% There was a very small fraction of O and Fe associated with this event.
2. The SEP event was characterized by a distinctive velocity dispersion. Protons with energies >100 keV arrived about 6 hr before those with energies <40 keV. The earliest arriving particles are anisotropic, coming from the sunward direction. The magnetic field during the time preceding their arrival was radial, indicating the particles are moving along radial magnetic field lines from their source to *PSP*.
3. The onset of the highest energy particles associated with the SEP event occurred at about 2:00 UT on 2018–315. At this time, a CME, seen in STA/C2 images, was seen to be moving away from the Sun. The CME arrived at *PSP* about a day after the onset of the SEP event. The CME was moving directly toward *PSP*.
4. There was no shock associated with the CME observed locally by *PSP*. Separate modeling of the event also suggests there was no shock during its evolution from the Sun to *PSP*, although a weak subcritical quasi-perpendicular shock with an FM Mach number less than 2 may have existed over an extended region at one flank of the CME.
5. The ion flux versus time at each energy is characterized by a rather gradual rise from the event onset to the peak over a period of 2–8 hr, depending on the energy. Above 100 keV, the time to maximum is about 2 hr later than the event onset, while at about 30 keV, the difference is nearly 8 hr.
6. The event-averaged differential flux spectrum has a nearly power-law dependence on energy with a spectral index between −4 and −5. This is consistent with $f \propto p^{-10\ \mathrm{to}\ -12}$, where f is the phase-space density and p is the momentum. The spectrum evolved with time throughout the event.
7. The onset time of the earliest arriving higher energy ions is consistent with them originating at the CME, when it was at $7.4R_{\odot}$, and moving without scattering to *PSP*. The path length of the ions is found to be 0.21 au. In contrast, ions below about 50 keV arrive later, by about 2–4 hr, compared with the time expected from scatter-free transport. The derived path length of these ions ranges from 0.32 to 0.38 au, nearly twice that of the high-energy ions.
8. The observed ion fluxes can be reasonly fit to solutions to the Parker transport equation, which assumes a quasi-isotropic pitch-angle distribution and includes diffusion, advection, and energy change in the solar wind. The model assumed a source comoving with the CME with a power-law dependence on momentum with a spectral index consistent with the observed event-averaged spectrum. The source was also assumed to have a duration of a few hours, depending on the ion energy. The source of higher energy ions has a shorter duration than lower energy ions. The model is spherically symmetric. The parallel diffusion coefficient that best fit the data has the form $\kappa = 2.7 \times 10^{17}(r/r_0)^2(E/E_0)^{9/8}$, where $r_0 = 7.4R_{\odot}$ and $E_0 = 10$ keV.

Based on the above conclusions, we offer the following interpretation. As the CME erupted and began moving away from the Sun from about 19:30 UT on DOY 314 to about 1:00 UT on DOY 315 ($3R_{\odot}$–$7.4R_{\odot}$), it drove a plasma

compression, or a weak shock with a Mach number of about 1.3, which accelerated particles to over a few hundred keV with an $f \propto p-11$ phase-space distribution function (p is the magnitude of the particle momentum) at the shock/compression. The CME continued to accelerate particles for a few hours longer, but with an acceleration rate that decreased with time so that higher energy ions were created with less efficiency, although lower energy ions were still being produced. After a few hours, the CME no longer accelerated particles. Because they are faster than the CME, the particles propagated ahead of the CME, in the nearly radial interplanetary magnetic field, and were detected by *PSP*/IS⊙IS/EPI-Lo well before the CME arrived at *PSP*. The earliest arriving high-energy particles arrived to *PSP* with little pitch-angle scattering in the turbulent interplanetary magnetic field. Lower energy ions arrived later because they were scattered in the interplanetary field more effectively than the higher energy ions. We suggest that IS⊙IS/EPI-Lo did not detect the earliest arriving, scatter-free, low-energy ions because their intensity is below the background. This picture is consistent with a very weak gradual event without an associated ESP (locally observed shock-related) component. Other interpretations, such as that offered in a companion paper (Mitchell et al. 2020), may also be consistent with the observations.

In previous observations at 1 au, there is considerable variability in the peak SEP intensity as a function of CME speed, but generally there is a higher SEP intensity for faster CMEs (Kahler 2001; Desai & Giacalone 2015). Figure 1 of Kahler (2001) shows the peak intensity of 2 and 20 MeV protons as a function of CME speed. Although we observed no particles associated with this event at these energies, we can extrapolate our results to higher energies and to 1 au to compare. We note that no 1 au spacecraft observed this event. The peak intensity of ∼200 keV (mostly) protons in this event was approximately 0.1 cm^{-2} s^{-1} sr^{-1} keV^{-1}. The observed event-averaged spectrum had a power-law dependence on energy with a spectral index of −4.7. Thus, at 2 MeV we would expect the intensity to be approximately $10^{-5.7}$ cm^{-2} s^{-1} sr^{-1} keV^{-1}, or $10^{-2.7}$ cm^{-2} s^{-1} sr^{-1} MeV^{-1}, the units used in Kahler's Figure 1. The CME speed for this event was 360 km s^{-1}. These values would appear on the Kahler's plot but would be among the weakest he studied. Moreover, this event occurred at about 0.25 au, and not at 1 au where the events used in his study were observed. An upper bound to this extrapolation would be a simple $1/r^2$ dependence, or a reduction by a factor of 16, which would place this point at the bottom axis of Kahler's figure. Because the spectrum of this event is so steep, the radial dependence is likely much stronger than $1/r^2$, meaning that this event would be so weak as to not appear on his figure.

A couple of aspects of this event are worth emphasizing. It is unique because it is the closest to the Sun in which a CME-related SEP event has been observed. Moreover, it represents an example of a very weak gradual event without an associated ESP event (at any energy). The peak intensities occurred well before the arrival of the CME, and there was no CME-driven shock observed locally by *PSP*. We were fortunate that the weak solar cycle during which this event occurred led to a very quiet background, allowing for these observations and analysis and providing a unique opportunity to study particle transport close to the Sun.

Parker Solar Probe was designed, built, and is now operated by the Johns Hopkins Applied Physics Laboratory as part of NASA's Living with a Star (LWS) program (contract NNN06AA01C). Support from the LWS management and technical team has played a critical role in the success of the *Parker Solar Probe* mission. J.G. acknowledges useful conversations about the Parker transport equation with J. Kota and F. Fraschetti. A.K. and A.P.R. acknowledge financial support from the ANR project COROSHOCK ANR-17-CE31-0006-01 and from the ERC project SLOW_SOURCE—DLV-819189. We thank Jon Linker and Pete Riley of Predictive Sciences for providing the background solar wind model exploited in this study. The STA/C2 images, which were analyzed for results presented in this paper, were obtained from the STEREO science center.

ORCID iDs

D. G. Mitchell https://orcid.org/0000-0003-1960-2119
R. C. Allen https://orcid.org/0000-0003-2079-5683
M. E. Hill https://orcid.org/0000-0002-5674-4936
J. R. Szalay https://orcid.org/0000-0003-2685-9801
M. I. Desai https://orcid.org/0000-0002-7318-6008
D. J. McComas https://orcid.org/0000-0001-6160-1158
E. R. Christian https://orcid.org/0000-0003-2134-3937
N. A. Schwadron https://orcid.org/0000-0002-3737-9283
S. Bale https://orcid.org/0000-0002-1989-3596
A. Case https://orcid.org/0000-0002-3520-4041
C. Joyce https://orcid.org/0000-0002-3841-5020
J. C. Kasper https://orcid.org/0000-0002-7077-930X
K. G. Klein https://orcid.org/0000-0001-6038-1923
K. Korreck https://orcid.org/0000-0001-6095-2490
R. A. Leske https://orcid.org/0000-0002-0156-2414
R. J. MacDowall https://orcid.org/0000-0003-3112-4201
W. H. Matthaeus https://orcid.org/0000-0001-7224-6024
T. Nieves-Chinchilla https://orcid.org/0000-0003-0565-4890
M. Pulupa https://orcid.org/0000-0002-1573-7457
M. L. Stevens https://orcid.org/0000-0002-7728-0085
A. Szabo https://orcid.org/0000-0003-3255-9071

References

Axford, W. I., Leer, E., & Skadron, G. 1977, Proc. ICRC, 11, 132
Bale, S. B., Badman, S. T., Bonnell, J. W., et al. 2019, Natur, 576, 237
Bale, S. B., Goetz, K., Harvey, P. R., et al. 2016, SSRv, 204, 49
Bandyopadhyay, R., Matthaeus, W. H., Parashar, T. N., et al. 2020, ApJS, doi:10.3847/1538-4365/ab6220
Barnes, C. W., & Simpson, J. A. 1976, ApJL, 210, L91
Beeck, J., & Sanderson, T. R. 1989, JGR, 94, 8769
Bell, A. R. 1978, MNRAS, 182, 147
Blandford, R. D., & Ostriker, J. P. 1978, ApJL, 221, L29
Bryant, D. A., Cline, T. J., Desai, U. D., & McDonald, F. B. 1962, JGR, 67, 4983
Cliver, E. W. 2016, ApJ, 832, 128
Desai, M. I., & Giacalone, J. 2016, LRSP, 13, 3
Desai, M. I., Mitchell, D. G., Szalay, J. R., et al. 2020, ApJS, doi:10.3847/1538-4365/ab65ef
Droge, W., Kartavykh, Y. Y., Klecker, B., & Kovaltsov, G. A. 2010, ApJ, 709, 912
Drury, L. 1983, RPPh, 46, 973
Forman, M. A., & Drury, L. 1983, Proc. ICRC, 2, 267
Fox, N. J., Velli, M. C., Bale, S. D., et al. 2016, SSRv, 204, 7
Giacalone, J. 2012, ApJ, 761, 28
Giacalone, J. 2015, ApJ, 799, 80
Giacalone, J., & Jokipii, J. R. 1999, ApJ, 520, 204
Giacalone, J., & Jokipii, J. R. 2004, ApJ, 616, 573
Giacalone, J., Jokipii, J. R., & Kota, J. 2002, ApJ, 573, 845

Giacalone, J., Jokipii, J. R., & Kota, J. 2005, GMS, 156, 41
Gleeson, L. J., & Axford, W. I. 1968, Ap&SS, 2, 431
Gloeckler, G., Ipavich, F. M., Klecker, B., Hovestadt, D., & Scholer, M. 1985, Proc. ICRC, 4, 182
Gosling, J. T. 1993, JGR, 98, 18937
Gosling, J. T., Asbridge, J. R., Bame, S. J., et al. 1981, JGR, 86, 547
Hill, M. E., Mitchell, D. G., Allen, R. C., et al. 2020, ApJS, doi:10.3847/1538-4365/ab643d
Hill, M. E., Mitchell, D. G., Andrews, G. B., et al. 2017, JGR, 122, 1513
Howard, R., Vourlidas, A., Bothmer, B., et al. 2019, Natur, 576, 232
Jokipii, J. R. 1966, ApJ, 255, 716
Jokipii, J. R. 1982, ApJ, 146, 480
Jokipii, J. R. 1992, in AIP Conf. Ser. 264, Particle Acceleration in Cosmic Plasmas, ed. G. P. Zank & T. K. Gaisser (Melville, NY: AIP), 137
Jokipii, J. R., & Parker, E. N. 1969, PhRvL, 21, 44
Kahler, S. 1992, ARA&A, 30, 113
Kahler, S. 2001, JGR, 106, 20947
Kahler, S. W., Hildner, E., & Van Hollebeke, M. A. I. 1978, SoPh, 57, 429
Kahler, S. W., Sheeley, N. R., Jr., Howard, R. A., et al. 1984, JGR, 89, 9683
Kasper, J. C., Abiad, R., Austin, G., et al. 2016, SSRv, 204, 131
Kasper, J. C., Bale, S. D., Belcher, J. W., et al. 2019, Natur, 576, 228
Kennel, C. F., Coroniti, F. V., Scarf, F. L., et al. 1986, JGR, 91, 11917
Kota, J. 2000, JGR, 105, 2403
Kouloumvakos, A., Rouillard, A. P., Wu, Y., et al. 2019, ApJ, 876, 80
Krymsky, G. F. 1977, DoSSR, 234, 1306
Lario, D., Ho, G. C., Decker, R. B., et al. 2003, in AIP Conf. Proc. 679, SOLAR WIND 10, ed. M. Velli (Melville, NY: AIP), 640
Lee, M. A. 1983, JGR, 88, 6109
Lee, M. A. 2005, ApJ, 158, 38
Lee, M. A., Mewaldt, R. M., & Giacalone, J. 2012, SSRv, 173, 247
Lionello, R., Linker, J. A., & Mikić, Z. 2009, ApJ, 690, 902
Mason, G. M., Mazur, J. E., Looper, M. D., & Mewaldt, R. A. 1995, ApJ, 452, 901
McComas, D., Alexander, N., Angold, N., et al. 2016, SSRv, 204, 187
McComas, D., Christian, E. R., Cohen, C. M. S., et al. 2019, Natur, 576, 223
McDonald, F. B., Teegarden, B. J., Trainor, J. H., & von Rosenvinge, T. T. 1976, ApJL, 203, L149
Mitchell, D. G., Giacalone, J., Allen, R. C., et al. 2020, ApJS, doi:10.3847/1538-4365/ab63cc
Nieves-Chinchilla, T., Szabo, A., Korreck, K. E., et al. 2020, ApJS, doi:10.3847/1538-4365/ab61f5
Palmer, I. D. 1982, RvGeo, 20, 335
Parker, E. N. 1965, P&SS, 13, 9
Pei, C., Jokipii, J. R., & Giacalone, J. 2006, ApJ, 641, 1222
Rao, U. R., McCracken, K. G., & Bukata, R. P. 1967, JGR, 72, 4325
Reames, D. V. 1999, SSRv, 90, 413
Riley, P., Lionello, R., Linker, J. A., et al. 2011, SoPh, 274, 361
Rouillard, Kouloumvakos, A., Vourlidas, A., et al. 2020, ApJS, doi:10.3847/1538-4365/ab579a
Ruffalo, D. 1995, ApJ, 442, 861
Scholer, M., Hovestadt, D., Ipavich, F. M., & Gloeckler, G. 1983, JGR, 88, 1977
Schwadron, N. A., Bale, S., Bonnell, J., et al. 2020, ApJS, doi:10.3847/1538-4365/ab5527
Schwadron, N. A., Townsend, L., Kosarev, K., et al. 2010, SpWea, 8, S00E02
Tan, L. C., Mason, G. M., Gloeckler, G., & Ipavich, F. M. 1989, JGR, 94, 6552
van Nes, P., Reinhard, R., Sanderson, T. R., Wenzel, K.-P., & Zwickl, R. D. 1984, JGR, 89, 2122